Tunable Piezoresistivity of Nanographene Films for Strain Sensing

Jing Zhao,[†] Guole Wang,[†] Rong Yang,[†] Xiaobo Lu,[†] Meng Cheng,[†] Congli He,[†] Guibai Xie,[†,§] Jianling Meng,[†] Dongxia Shi,[†] and Guangyu Zhang*[,†,‡]

[†]Beijing National Laboratory for Condensed Matter Physics and Institute of Physics, Chinese Academy of Sciences, Beijing 100190, China, [‡]Collaborative Innovation Center of Quantum Matter, Beijing 100190, China, and [§]National Key Laboratory of Science and Technology on Space Microwave, China Academy of Space Technology (Xi'an), Xi'an 710100, China

ABSTRACT Graphene-based strain sensors have attracted much attention recently. Usually, there is a trade-off between the sensitivity and resistance of such devices, while larger resistance devices have higher energy consumption. In this paper, we report a tuning of both sensitivity and resistance of graphene strain sensing devices by tailoring graphene nanostructures. For a typical piezoresistive nanographene film with a sheet resistance of ~100 KΩ/□, a gauge factor of more than 600 can be achieved, which is 50× larger than those in previous studies. These films with high sensitivity and low resistivity were also transferred on flexible substrates for device integration for force mapping. Each device shows a high gauge factor of more than 500, a long lifetime of more than 10^4 cycles, and a fast response time of less than 4 ms, suggesting a great potential in electronic skin applications.

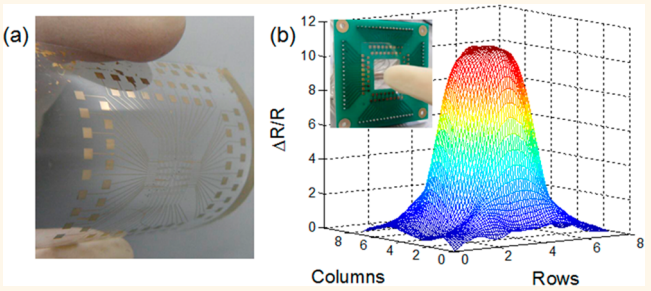

KEYWORDS: graphene · ultrasensitivity · controllable size · tunneling effect · artificial electronic skin

Graphene, the first isolated 2D material, has attracted more attention in many kinds of sensor applications owning to its ultrathin structure and novel mechanical, electrical, and chemical properties, such as magnetic,[1,2] chemical sensing,[3−5] photodetecting,[6−8] and others.[9,10] One of the most interesting is that graphene is an ideal material for flexible electronics such as strain sensing.[11−14] Compared with typical strain sensors based on metal,[15,16] semiconductors,[17−20] and polymers,[21,22] graphene-based strain sensors have advantages due to its ultrathin and transparent nature. Perfect graphene for strain sensing has low sensitivity, which is usually characterized by its gauge factor (GF), due to its zero band gap.[23−25] A band gap could be opened in graphene under high uniaxial strain (>23%);[26] however, irreversible structural damage is also likely to be induced under such high strain. In order to increase the sensitivity of a graphene strain sensor, certain structural engineering is required. Previously, we reported a new type of strain sensor based on quasi-continuous nanographene films in which charge carrier transport occurred *via* tunneling, resulting in a very high sensitivity.[27] However, such nanographene films with high GF (~300) are usually very resistive, with a sheet resistance of 10^6 KΩ/□, thus limiting their applications at low operating voltages, and the GF cannot be improved further. In this paper, we demonstrate that the piezoresistive property of the quasi-continuous nanographene film can be tailored by the nanographene densities and lateral sizes. We found that the nanographene film with a smaller grain size and with a higher density offers more tunneling passageways and larger average tunneling distance. As a result, we fabricated nanographene strain sensors with tunable GFs (~$10-10^3$) and sheet resistances (~$10-10^2$ KΩ/□). Moreover, we also demonstrate the use of such sensitive and conductive nanographene films for integrated strain sensor devices for real-time and spatially resolved monitoring of external stress distribution, suggesting a promising route toward artificial electronic skin and touch panels.

* Address correspondence to gyzhang@aphy.iphy.ac.cn.

Received for review November 6, 2014 and accepted February 4, 2015.

Published online February 04, 2015
10.1021/nn506341u

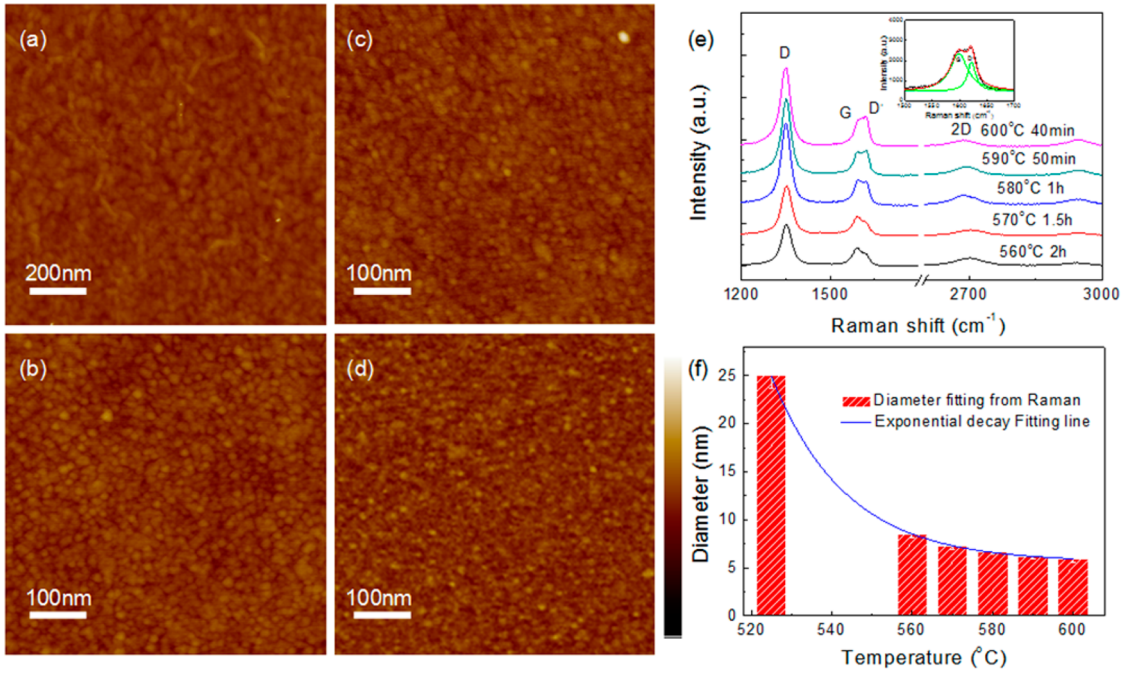

Figure 1. Grain sizes of NG with different growth temperature. Atomic force image of NG with the same sheet resistance of ~100 KΩ/□. With the same pressure ~0.2 Torr and plasma power of 100 W, the temperature and growth time is (a) 525 °C, 3 h (citing from ref 27) (b) 560 °C, 2 h; (c) 580 °C, 1 h; and (d) 600 °C, 45 min. The scale bar is 10 nm. (e) Raman shift of the NG with a typical D ≈ 1350 cm^{-1}, G ≈ 1598 cm^{-1}, and 2D ≈ 2700 cm^{-1} peak. Besides, a D′ peak of ~1621 cm^{-1} here indicates the stress between grown graphene and the substrates. The inset image demonstrates the Lorentz fitting with G ≈ 1598 cm^{-1} and D′ ≈ 1621 cm^{-1}. (f) According to the value of I_D/I_G from (e), the diameter of nanographene can be calculated, and the output from ~25 to ~5 nm shows a typical exponential decay of diameter with the increase of growth temperature.

RESULTS AND DISCUSSION

Nanographene (NG) films were grown on SiO_2/Si and fluor-phlogopite mica substrates by a remote plasma-enhanced chemical vapor deposition (RPECVD) system.[28−30] We found that the NG nucleation density can be tuned by the growth temperatures. Figure 1a−d show a series of atomic force microscopy (AFM) images of four NG samples grown at 525, 560, 580, and 600 °C with pure methane as the precursor. The gas pressure is kept at 0.2 Torr and the plasma power is 100 W. In order to obtain a similar sheet resistance of ~100 KΩ/□, we used various growth times for the four samples of 3 h, 2 h, 1 h, and 45 min. Raman scattering was carried out for these samples to quantitatively access the average NG grain sizes (Figure 1e). The 2D peak at ~2700 cm^{-1} reflecting the sp^2 hybridization confirms the product of graphene,[31] while the high D peak at ~1350 cm^{-1} mainly comes from the graphene edges.[32] The peak at around 1600 cm^{-1} can be split into two peaks, *i.e.*, G (~1598 cm^{-1}) and D′ (~1621 cm^{-1}), as illustrated in the inset image of Figure 1e. Note that the D′ peak is also induced by the disorder.[33−35] The density ratio of these two peaks (I_D/I_G) varies with the growth temperature and time as well. We can fit the two peaks with a Lorenz line shape, and the grain size of nanographene (D) can be estimated by the following formula: $D = 560(I_D/I_G)^{-1}/E^4$,[36−38] where E is the Raman excitation laser energy with units of eV (E = 2.34 for a 532 nm excitation laser). The fitting results from I_D/I_G for these samples with a similar sheet resistance of ~100 kΩ/□ are shown in Figure 1e and f, respectively. The results from our previous study with growth carried out at 525 °C are also included.[27] We can see that the average grain size varies from ~25 nm to ~8 nm with the growth temperature increasing from 525 °C to 600 °C, and the correlation obeys an exponential decay law very well. According to our previous study, there was a competitive relationship between synthesizing and etching in this NG growth process.[30] When the growth temperature increases, the hydrogen etching effect is weakened, leading to higher nucleation density. For quasi-continuous films with a sheet resistance of ~100 kΩ/□, the grain size is inversely proportional to the nucleation density, which leads to varied original tunneling distance. Through controlling the different nucleation temperatures and growth times, a series of various GF devices with the same resistance can be obtained.

Employing these as-grown NG films as the starting materials, we fabricated a series of two-terminal devices using a shadow mask to deposit Ti(2 nm)/Au(30 nm) electrodes. The silver conducting epoxy was utilized to wire these devices for measurements. Electrical transport properties of these devices were measured at room temperature, and the change of the resistances with the applied strain can be real-time monitored. Figure 2a shows typical piezoresistive

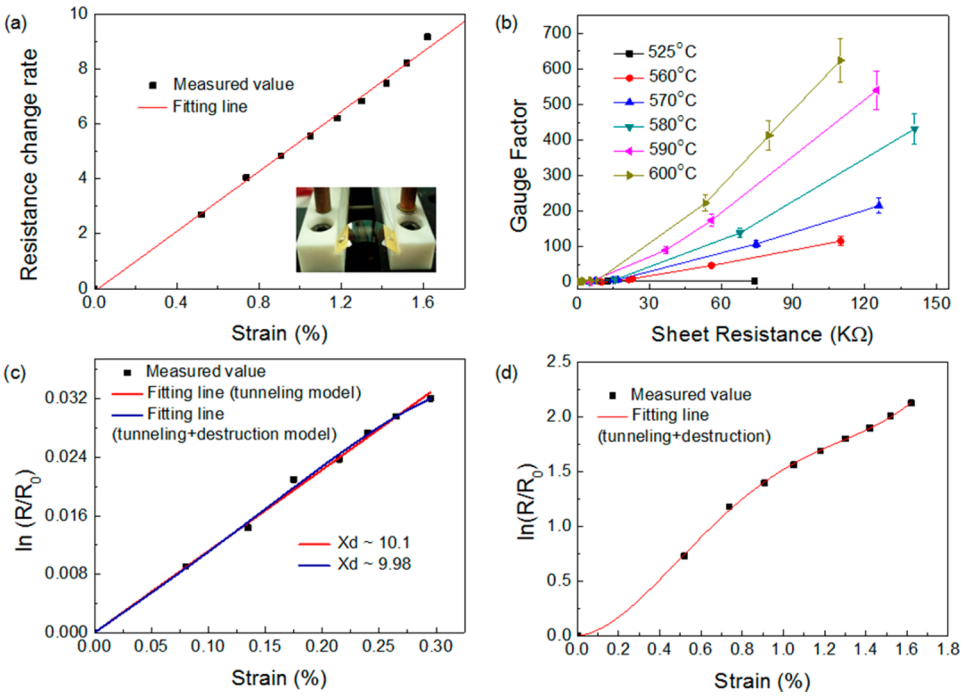

Figure 2. Piezoresistivity of the nanographene-based strain sensor devices. (a) Typical device's characteristic of resistance change rate with an increase in applied strain. When the strain was applied from 0% to ~1.6%, the resistance increases from 100 KΩ/□ to 1MΩ and the gauge factor can be calculated as ~546. The inset shows the optical image of the measurement setup. (b) GF *versus* sheet resistance for a series of NG samples at different growth temperatures. (c) 525 °C grown sample with a GF of ~11; the point is the measured value; the red and blue lines are the fitting lines according to tunneling and tunneling + destruction models, respectively. (d) 600 °C grown sample with a GF of ~546; the point and line data are the measured value and fitting line from the tunneling + destruction model, respectively.

properties of a device with nanographene grown at 600 °C for 45 min. The resistance changes linearly with the applied strain, and a GF of ~546 can be calculated from the standard calculation method described in ref 27. In addition, similar to the previous result,[27] the relationship between resistance change and strain is linear under both tensile and compressive strain. So the GF is stable under different strain and determined only by the original tunneling distance. Under compressive strain, devices' resistance decreases with the increasing stress, and this can be understood by the truncated tunneling distance under compressive stress. As shown in the AFM images in Figure 1, the nucleation density of NG is mainly determined by the growth temperature. At a fixed growth temperature, extended growth time would mainly increase the size of NG, leading to a reduced sheet resistance of the NG film, while under the same growth duration, a higher growth temperature would lead to a higher NG nucleation density (or lower sheet resistance). To characterize the influence of nucleation density on the sensitivity of the device, we measured a series of devices with different NG nucleation densities. GF as a function of the initial resistance is shown in Figure 2b for samples grown at different growth temperatures. We can see when the nucleation density (growth temperature) is fixed, the GF increases exponentially with the devices' initial resistances (decreasing the growth time). More important is that for samples with similar sheet resistances grown at different temperatures GF is proportional to the growth temperature or the nucleation density. As a result, devices with a large GF can be achieved for a low-resistance NG sample through adjusting the nucleation density instead of increasing the sheet resistance. Such highly sensitive strain-sensing devices with low resistances imply advantages in power consumption.

The piezoresistive effect in NG films can be ascribed to the tunneling of charged carries between adjacent NG sheets.[27] A film's sheet resistance increases exponentially when the average distance between NG sheets extends by an external applied strain. According to the Simmons function,[39,40] the relationship between the resistance R and average tunneling distance d can be given by[41,42]

$$R = \left[\frac{8\pi hL}{3A^2XdN}\right]e^{Xd} \quad (1)$$

$$X = \frac{4\pi(2m\varphi)^{1/2}}{h} \quad (2)$$

where N is the number of conducting paths and L is the number of particles within a conducting path; e, m, and h are the electron charge, mass, and the Plank constant, respectively; A^2 is the effective area; and φ is the barrier height between adjacent nanosheets. When the

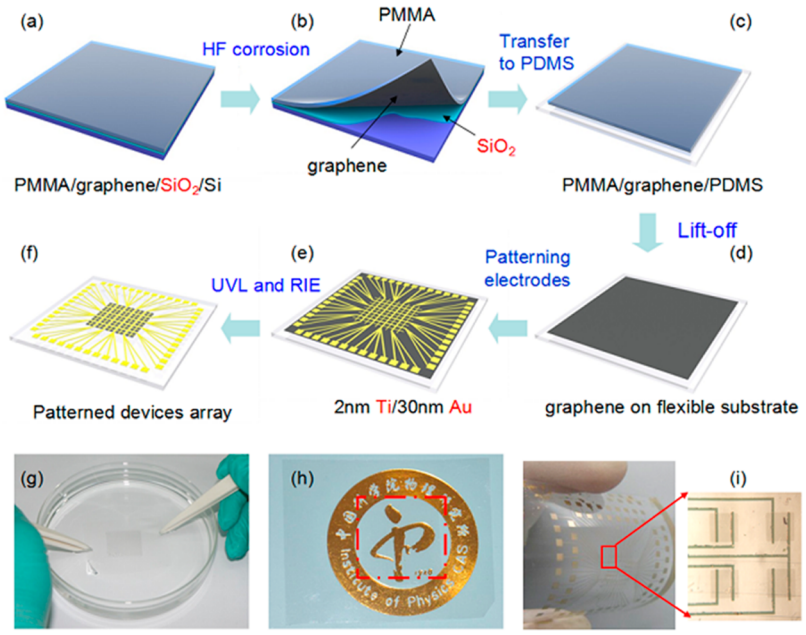

Figure 3. Schematic fabrication process of a device matrix for e-skin. (a) Spin-coating of 5% 950 PMMA on graphene/SiO_2/Si. (b) Soaking the samples in 10% HF in water to float off the PMMA/graphene film. (c) Transferring the PMMA/graphene film onto a flexible substrate and spin-coating with PMMA once more to decrease the wrinkling of graphene. (d) Removal of PMMA on the surface of graphene in acetone. (e) Patterning the electrodes by UV-lithograph, metal deposition, and lifting-off. (f) Removal of the excess graphene by RIE. (g) PMMA/graphene film floating on the surface of water after wet chemical etching, then received by a flexible substrate. (h) As-transferred graphene on PDMS (marked by the red dotted square) showing high transparency. (i) Optical image of e-skin with an 8 × 8 device array. The zoom-in image shows the typical two-terminal planar structure of the device. The gray area demonstrates a graphene film with a size of 500 × 500 μm.

strain is smaller than 0.3%, according to eqs 1 and 2, the resistance change rate along with the original tunneling distance d_0 and the strain ε can be described as

$$\ln\frac{R}{R_0} = \ln(1+\varepsilon) + Xd_0\varepsilon \quad (3)$$

While the strain is larger than 0.3%, the tunneling model is no longer applicable, replaced by the tunneling and destruction model in which N changes and can be described as[43]

$$N = N_0 \exp[-(\alpha\varepsilon + \beta\varepsilon^2 + \gamma\varepsilon^3 + \lambda\varepsilon^4)] \quad (4)$$

This equation implies that when the strain exceeds a certain limit, the conducting path conveniently decreases. Herein, eq 4 is modified by a tunneling and destruction model:

$$\ln\left(\frac{R}{R_0}\right) = \ln(1+\varepsilon) + \alpha\varepsilon + \beta\varepsilon^2 + \gamma\varepsilon^3 + \lambda\varepsilon^4 \quad (5)$$

In this model, the parameter α is equivalent to Xd_0. According to our previous study, the initial tunneling distance of the device grown at 525 °C can be estimated as d_0 = ~1 nm in view of X = ~10 nm^{-1}.[44] From Figure 2c, we can see that the two different models both fit very well when the strain is less than 0.3%, where Xd_0 and α are 10.1 and 9.98, respectively. For the samples grown at 600 °C, the relationship between the resistance change rate and strain is shown in Figure 2d. According to the theoretical result, the fitted α = ~14.2 indicates the tunneling distance is ~1.4 nm, which is larger than that grown at 525 °C. This result caused the sensitivities (GF) to be different from each other. By utilizing this tunneling and destruction model, the distance between NG sheets can be easily estimated as long as the piezoresistive properties of samples are known, and it is only determined by the sample itself.

A schematic diagram of the devices with different nucleation densities grown at 525 and 600 °C is shown in Figure S2 to illustrate the dependence of devices' sensitivity on the NG nucleation density. From the experimental results shown in Figure 2, we can deduce that with the same resistance the higher nucleation density sample with smaller NG sheets has a larger tunneling distance. Considering the strain is less than 0.3%, equation 1 can be deduced into

$$\mathrm{GF} = \frac{\Delta R}{R_0}/\varepsilon = \frac{1}{\varepsilon+\varepsilon^2}e^{X\Delta d} - \frac{1}{\varepsilon} \quad (6)$$

When the same strain is applied, the higher sensitivity corresponds to a more significant tunneling distance change, Δd. Since the strain $\varepsilon = \Delta d/d_0$, the initial distance between the NG sheets (d_0) was larger. From experimental results we can see the grain size of the nanographene is smaller and the tunneling distance is larger at 600 °C compared with the one grown at 525 °C, which is in accordance with the schematic diagram in Figure S2. These features support our understanding that increasing the nucleation density is an optimized access to improve the sensitivity instead of increasing the resistance blindly. Figure 2b also illustrates the

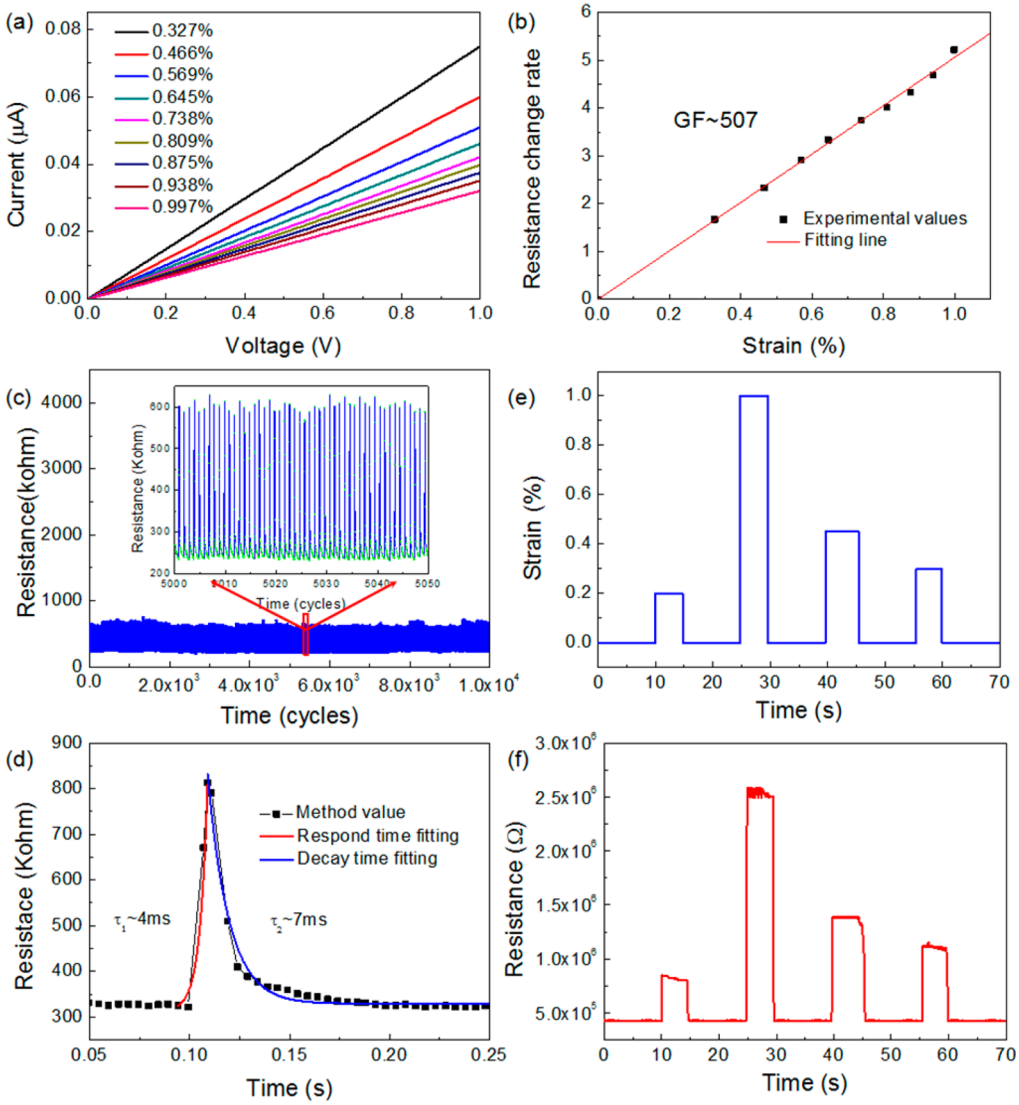

Figure 4. Piezoresistive properties of individual devices on PDMS. (a) *I*−*V* curve with different strain. (b) Normalized relationship between the resistance change rate and the applied strain, revealing a gauge factor of ∼507. (c) Real-time resistance change during 10 000 cycles of applying/releasing stress for a device. The inset is the zoom-in figure showing 50 cycles of measurements. (d) Time response characteristic of the artificial e-skin device. According to the fitting line, the response time (rise time) and decay time is ∼4 ms and ∼7 ms, respectively. (e) Series of strain pulses (0.2%, 1%, 0.45%, 0.3%) with time applied on the device. (f) Resistance change corresponding to the strain pulse in (e).

validity that a series of devices with a similar sheet resistance of ∼100 KΩ/□ can achieve a GF from ∼11 to ∼600 due to the growth temperature varying from 525 to 600 °C.

Considering the high sensitivity of this graphene-based strain sensor, it provides a feasible solution for artificial skins once we transferred the quasi-continuous film onto flexible substrates.[45] Figure 3a−f depicts the transfer and device fabrication process. After transferring the quasi-continuous NG film onto flexible substrates, contact electrodes (2 nm-Ti/40 nm-Au) of the two-terminal devices were defined by standard UV lithography (MA6, Karl Suss), metal deposition in an e-beam evaporator, and lifting-off techniques. Note that NG is everywhere on the substrates, and the removal of the excess graphene is necessary by a second UV lithography and oxygen plasma etching. Figure 3g shows an optical image of a PMMA/graphene film after it is released in water. This quasi-continuous graphene film can be placed on arbitrary substrates with few cracks and wrinkles. The transferred graphene on PDMS is positioned above the logo of "IOP" in Figure 3h, demonstrating good uniformity and transparency. Figure 3i is an optical image of an as-fabricated 8 × 8 device array with flexibility, and the zoom-in picture clearly shows the two-terminal planar structure. Raman spectra and an AFM image of the transferred graphene on PDMS are shown in Figure S3. The electrical characteristic of a typical device under tensile strain up to 1% is illustrated in Figure 4a and b, where panel a is the *I*−*V* curve under strain from 0.327% to 0.997%. Similar to the device before transferring, the resistance increased

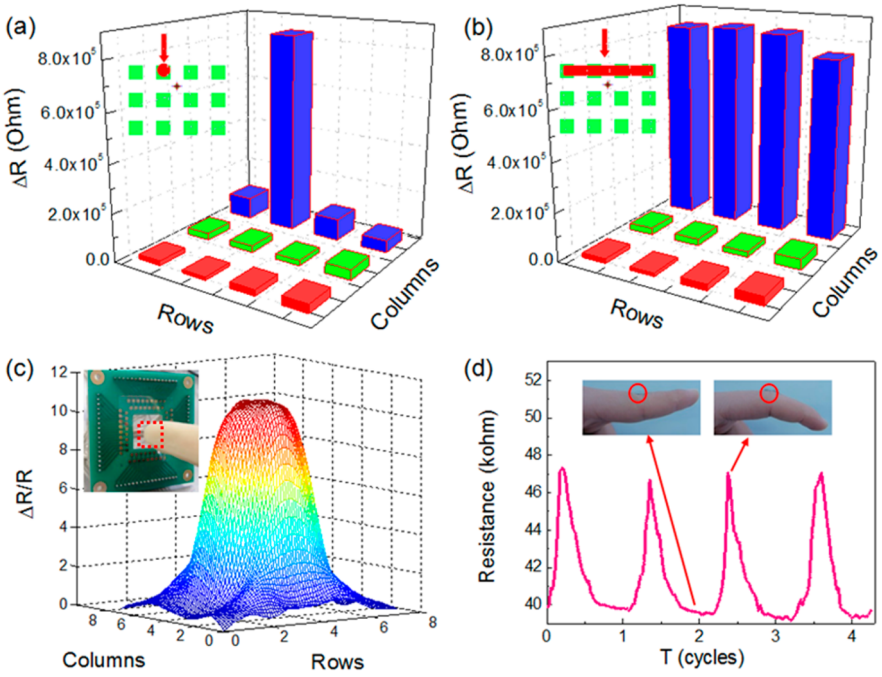

Figure 5. Multidimensional tactile sensing image of e-skin. (a, b) "Point"- and "line"-stress tests on a 3 × 4 device array. (c) Measurement of the electric response on applying finger touching (inset). The resistance change rate reflects the strain distribution. (d) Artificial electronic skin on a PDMS substrate attached on a finger to detect the movement of knuckles.

obviously with high strain. The linear relationship between resistance and strain is shown in Figure 4b, and the GF can be estimated as ~507. After 10 000 cycles of indentation, the initial resistance remains unchanged in Figure 4c, which illustrates this device is very robust and reliable. The inset in Figure 4c is the zoom-in data showing 50 cycles of resistance monitoring. Figure 4d demonstrates the real-time resistance response of a device when applying a series of pressure pulses with a periodicity of ~180 ms. The response speed of the device can be extracted from exponential functions with the rise (Γ_{rise}) and decay time (Γ_{decay}) of ~4 ms and ~7 ms, respectively. Such a response time is much shorter than those reported in previous studies or that of real human skin (~30−50 ms).[46,47] Various strain pulses applied on the device in Figure 4e can generate resistance change (Figure 4f). In addition, a series of strains applied to the device can be monitored (Figure S4d), providing a possible application in a large stress range.

The space-resolved piezoresistive effect of the integrated devices within a working area of less than 1 × 1 cm^2 on a flexible substrate is shown in Figure 5. Pulsed pressing was applied from the back-side of the device by a metal indenter to introduce a local strain, and the device's real-time resistance was monitored during testing. A switch matrix was used to output the resistances of all devices on the chip simultaneously. Figure 5a and b demonstrate the resistance variation of the 3 × 4 device array when "point" and "line" forces were afforded, respectively. The inset sketch diagrams separately display the real-space distribution of the device (green color), while the red color points to the position where outside stimuli occur. We can see that the resistance of an individual device changes obviously only if local stress is applied. More detailed information can be seen in Figure S5. To further reveal the high spatial resolution of this integrated graphene strain sensor for artificial e-skin, we fabricated an 8 × 8 device array on a 1 mm thick PDMS film for "area" touch tests. Devices were separated by 500 μm from each other. This PDMS film with devices was attached to a printed circuit board with a square hole (inset of Figure 5c). The device array can map the applied inhomogeneous strain to the PDMS film as each device works as a pixel. Figure 5c shows the resulting resistance change mapping for the device array upon a gentle fingertip touch on the back-side of the PDMS film. The inset image demonstrates the progress of applying finger touch on the e-skin. The *x*- and *y*-coordinates represent the relative position of the devices. When the fingertip touched the device area, the resistance change of individual devices was mapped out, showing high sensitivity with a space resolution. The force per unit area suffered can be calculated as $\sigma = Y\varepsilon$, where Y and ε represent the Young modulus and strain, respectively. The Young modulus of the PDMS is ~7.5 × 10^5 Pa. The strain caused by finger touch at the center is estimated to be ~2% from Figure 5c, according to the resistance change rate. Thus, we obtained σ = ~15 kPa, a resistance change rate reflecting the sensitivity, which can be compared to a real human finger. Such e-skin devices can be potentially used to recognize fingerprints if integrating a high density of the device array. In addition, these

e-skin devices can be easily attached to the body surface to monitor movement, as they are highly elastic and stretchable. Figure 5d demonstrates the resistance change of one device with movement of the little knuckles.

CONCLUSION

In this study, we systematically explored the piezoresistive dependence of various quasi-continuous NG films. We found that the NG nucleation density and grain size can be controlled by the growth temperature. With the temperature varied from 525 °C to 600 °C, the grain size decreased from 25 nm to 8 nm, which can be estimated by the intensity of I_D/I_G in the Raman shift. The different nucleation provides various initial tunneling distances between NG sheets, which leads to the GF of devices differing from 10 to 10^3 with the same resistance. The device with a higher nucleation density possesses a larger tunneling distance, causing a higher GF compared with the lower nucleation density device under the same conditions. A gauge factor of more than 600 of the device grown at 600 °C with a sheet resistance of ~100 KΩ/□ can be achieved, whose GF is 50× larger than the one grown at 525 °C. Thus, we can improve the GF significantly through tuning the temperature to increase the nucleation density of the NG. This density-dependent piezoresistive property provides a way to obtain a highly sensitive graphene-based strain sensor through increasing the NG density rather than the initial sheet resistance. We also demonstrate the use of such NG strain sensors with high sensitivity and low resistance for e-skin applications. Each device has good quality: a gauge factor of more than 500, a long lifetime of more than 10 000 cycles, a fast respond speed of less than a few milliseconds, and high spatial resolution, which shows great potential in future robotic and bionic applications as well as thin-film flexible electronics such as touch screens. Moreover, the present study also suggests a route toward fully transparent e-skin with large domain sized graphene as electrodes and nanographene as sensing materials.

METHODS

Raman Characterization. Raman spectra were collected in a Lab RAMHR-800 Raman system with a laser excitation of $\lambda = 532$ nm, a power of ~0.6 mW, and a beam spot size of ~1 μm.

Transfer of Graphene onto Flexible Substrates. Poly(methyl methacrylate) (PMMA, 950 K, 5% in anisole) was first spin-coated on the film, then baked at 180 °C for 3 min. This process was usually repeated two or three times to obtain a PMMA thickness of ~1 μm. The coated sample was then soaked in 10% hydrofluoric acid (HF) in water for a few minutes to float off the PMMA/graphene layer by water intervention. Repeated rinsing in deionized water of this floating film is needed to fully remove the HF residue. The floating film was then received on flexible substrates such as polydimethylsiloxane (PDMS) or polythylene terephthalate (PET), blow-dried by nitrogen, then baked at 80 °C for a few minutes to remove excess water. Additional PMMA coating was carried out to reduce the wrinkles formed during the transfer process and finally removed in hot (70 °C) acetone.

Device Fabrications. After transferring the nanographene film to the flexible substrate, S1813 resist was spin-coated at 4500 rpm on it (baking 1 min at 115 °C), and then the standard UV lithography (MA6, Karl Suss) was carried with an exposure time of ~12 s and a developing time of ~40 s (MF-319). Then 2 nm Ti/40 nm Au was deposited by e-beam evaporation on graphene as the contact electrodes. To remove the excess graphene, we executed a second UV lithography and then O_2-plasma etching, which was carried out in a reactive ion etching system (Plasma Lab 80 Plus, Oxford Instruments Company). With 100 sccm O_2 as precursor, the plasma power and pressure are 100 W and 0.1 Torr, respectively. The etching time is ~13 s.

Conflict of Interest: The authors declare no competing financial interest.

Supporting Information Available: The Raman shift of the samples with different growth conditions; schematic diagram of the tunneling mechanism with different growth temperatures; Raman spectroscopy and AFM image of the nanographene on PDMS after transfer; and electrical properties of nanographene-based artificial electronic skin. This material is available free of charge *via* the Internet at http://pubs.acs.org.

Acknowledgment. This work was supported by the National Basic Research Program of China (973 Program, grant nos. 2013CB934500, 2012CB921302, and 2013CBA01602), the National Science Foundation of China (NSFC, grant nos. 91223204, 61325021, 61390503, 11204358, and 11174333), and Strategic Priority Research Program (B) of the Chinese Academy of Sciences (grant no. XDB07010100).

REFERENCES AND NOTES

1. Pisana, S.; Braganca, P. M.; Marinero, E. E.; Gurney, B. A. Graphene Magnetic Field Sensors. *IEEE Trans. Magn.* **2010**, *46*, 1910–1913.
2. Tombros, N.; Jozsa, C.; Popinciuc, M.; Jonkman, H. T.; van Wees, B. J. Electronic Spin Transport and Spin Precession in Single Graphene Layers at Room Temperature. *Nature* **2007**, *448*, 571–U4.
3. Schedin, F.; Geim, A. K.; Morozov, S. V.; Hill, E. W.; Blake, P.; Katsnelson, M. I.; Novoselov, K. S. Detection of Individual Gas Molecules Adsorbed on Graphene. *Nat. Mater.* **2007**, *6*, 652–655.
4. Wehling, T. O.; Novoselov, K. S.; Morozov, S. V.; Vdovin, E. E.; Katsnelson, M. I.; Geim, A. K.; Lichtenstein, A. I. Molecular Doping of Graphene. *Nano Lett.* **2008**, *8*, 173–177.
5. Ohno, Y.; Maehashi, K.; Yamashiro, Y.; Matsumoto, K. Electrolyte-Gated Graphene Field-Effect Transistors for Detecting pH Protein Adsorption. *Nano Lett.* **2009**, *9*, 3318–3322.
6. Bonaccorso, F.; Sun, Z.; Hasan, T.; Ferrari, A. C. Graphene Photonics and Optoelectronics. *Nat. Photonics* **2010**, *4*, 611–622.
7. Park, J.; Ahn, Y. H.; Ruiz-Vargas, C. Imaging of Photocurrent Generation and Collection in Single-Layer Graphene. *Nano Lett.* **2009**, *9*, 1742–1746.
8. Xia, F. N.; Mueller, T.; Lin, Y. M.; Valdes-Garcia, A.; Avouris, P. Ultrafast Graphene Photodetector. *Nat. Nanotechnol.* **2009**, *4*, 839–843.
9. Sakhaee-Pour, A.; Ahmadian, M. T.; Vafai, A. Applications of Single-Layered Graphene Sheets as Mass Sensors and Atomistic Dust Detectors. *Solid State Commun.* **2008**, *145*, 168–172.
10. Wong, C. L.; Annamalai, M.; Wang, Z. Q.; Palaniapan, M. Characterization of Nanomechanical Graphene Drum Structures. *J. Micromech. Microeng.* **2010**, *20*, 1–12.

11. Novoselov, K. S.; Geim, A. K.; Morozov, S. V.; Jiang, D.; Zhang, Y.; Dubonos, S. V.; Grigorieva, I. V.; Firsov, A. A. Electric Field Effect in Atomically Thin Carbon Films. *Science* **2004**, *306*, 666–669.
12. Novoselov, K. S.; Geim, A. K.; Morozov, S. V.; Jiang, D.; Katsnelson, M. I.; Grigorieva, I. V.; Dubonos, S. V.; Firsov, A. A. Two-Dimensional Gas of Massless Dirac Fermions in Graphene. *Nature* **2005**, *438*, 197–200.
13. Geim, A. K.; Novoselov, K. S. The Rise of Graphene. *Nat. Mater.* **2007**, *6*, 183–191.
14. Geim, A. K. Graphene: Status and Prospects. *Science* **2009**, *324*, 1530–1534.
15. Rolnick, H. Tension Coefficient of Resistance of Metals. *Phys. Rev.* **1930**, *36*, 0506–0512.
16. Bridgman, P. W. Some Properties of Single Metal Crystals. *Proc. Natl. Acad. Sci. U.S.A.* **1924**, *10*, 411–415.
17. Kanda, Y. A Graphical Representation of the Piezoresistance Coefficients in Silicon. *IEEE Trans. Electron. Devices* **1982**, *29*, 64–70.
18. Richter, J.; Hansen, O.; Larsen, A. N.; Hansen, J. L.; Eriksen, G. F.; Thomsen, E. V. Piezoresistance of Silicon and Strained $Si_{0.9}Ge_{0.1}$. *Sens. Actuators A* **2005**, *123*, 388–396.
19. Grow, R. J.; Wang, Q.; Cao, J.; Wang, D. W.; Dai, H. J. Piezoresistance of Carbon Nanotubes on Deformable Thin-Film Membranes. *Appl. Phys. Lett.* **2005**, *86*, 093104.
20. Toriyama, T.; Funai, D.; Sugiyama, S. Piezoresistance Measurement on Single Crystal Silicon Nanowires. *J. Appl. Phys.* **2003**, *93*, 561–565.
21. Flandin, L.; Brechet, Y.; Cavaille, J. Y. Electrically Conductive Polymer Nano Composites as Deformation Sensors. *Compos. Sci. Technol.* **2001**, *61*, 895–901.
22. Cochrane, C.; Koncar, V.; Lewandowski, M.; Dufour, C. Design and Development of a Flexible Strain Sensor for Textile Structures Based on a Conductive Polymer Composite. *Sensors* **2007**, *7*, 473–492.
23. Fu, X. W.; Liao, Z. M.; Zhou, J. X.; Zhou, Y. B.; Wu, H. C.; Zhang, R.; Jing, G. Y.; Xu, J.; Wu, X. S.; Guo, W. L.; Yu, D. P. Strain Dependent Resistance in Chemical Vapor Deposition Grown Graphene. *Appl. Phys. Lett.* **2011**, *99*, 21307.
24. Huang, M. Y.; Pascal, T. A.; Kim, H.; Goddard, W. A.; Greer, J. R. Electronic-Mechanical Coupling in Graphene from *in Situ* Nanoindentation Experiments and Multiscale Atomistic Simulations. *Nano Lett.* **2011**, *11*, 1241–1246.
25. Lee, Y.; Bae, S.; Jang, H.; Jang, S.; Zhu, S. E.; Sim, S. H.; Song, Y. I.; Hong, B. H.; Ahn, J. H. Wafer-Scale Synthesis and Transfer of Graphene Films. *Nano Lett.* **2010**, *10*, 490–493.
26. Jin, C. H.; Lan, H. P.; Peng, L. M.; Suenaga, K.; Iijima, S. Deriving Carbon Atomic Chains from Graphene. *Phys. Rev. Lett.* **2009**, *102*, 205501.
27. Zhao, J.; He, C. L.; Yang, R.; Shi, Z. W.; Cheng, M.; Yang, W.; Xie, G. B.; Wang, D. M.; Shi, D. X.; Zhang, G. Y. Ultra-Sensitive Strain Sensors Based on Piezoresistive Nanographene Films. *Appl. Phys. Lett.* **2012**, *101*, 063112.
28. Yang, W.; He, C. L.; Zhang, L. C.; Wang, Y.; Shi, Z. W.; Cheng, M.; Xie, G. B.; Wang, D. M.; Yang, R.; Shi, D. X.; Zhang, G. Y. Growth, Characterization, and Properties of Nanographene. *Small* **2012**, *8*, 1429–1435.
29. Zhang, L. C.; Shi, Z. W.; Wang, Y.; Yang, R.; Shi, D. X.; Zhang, G. Y. Catalyst-Free Growth of Nanographene Films on Various Substrates. *Nano. Res.* **2011**, *4*, 315–321.
30. Liu, D. H.; Yang, W.; Zhang, L. C.; Zhang, J.; Meng, J. L.; Yang, R.; Zhang, G. Y.; Shi, D. X. Two-Step Growth of Graphene with Separate Controlling Nucleation and Edge Growth Directly on SiO_2 Substrates. *Carbon* **2014**, *72*, 387–392.
31. Dresselhaus, M. S.; Jorio, A.; Hofmann, M.; Dresselhaus, G.; Saito, R. Perspectives on Carbon Nanotubes and Graphene Raman Spectroscopy. *Nano Lett.* **2010**, *10*, 751–758.
32. Ferrari, A. C. Raman Spectroscopy of Graphene and Graphite: Disorder, Electron-Phonon Coupling, Doping and Nonadiabatic Effects. *Solid State Commun.* **2007**, *143*, 47–57.
33. Dresselhaus, M. S.; Dresselhaus, G.; Jorio, A.; Souza, A. G.; Saito, R. Raman Spectroscopy on Isolated Single Wall Carbon Nanotubes. *Carbon* **2002**, *40*, 2043–2061.
34. Saito, R.; Jorio, A.; Souza, A. G.; Dresselhaus, G.; Dresselhaus, M. S.; Pimenta, M. A. Probing Phonon Dispersion Relations of Graphite by Double Resonance Raman Scattering. *Phys. Rev. Lett.* **2002**, *88*, 027401.
35. Nemanich, R.; Solin, S. First- and Second-Order Raman Scattering from Finite-Size Crystals of Graphite. *Phys. Rev. B* **1979**, *20*, 392.
36. Knight, D. S.; White, W. B. Characterization of Diamond Films by Raman-Spectroscopy. *J. Mater. Res.* **1989**, *4*, 385–393.
37. Cancado, L. G.; Takai, K.; Enoki, T.; Endo, M.; Kim, Y. A.; Mizusaki, H.; Jorio, A.; Coelho, L. N.; Magalhaes-Paniago, R.; Pimenta, M. A. General Equation for the Determination of the Crystallite Size L-a of Nanographite by Raman Spectroscopy. *Appl. Phys. Lett.* **2006**, *88*, 3106.
38. Cancado, L. G.; Jorio, A.; Ferreira, E. H. M.; Stavale, F.; Achete, C. A.; Capaz, R. B.; Moutinho, M. V. O.; Lombardo, A.; Kulmala, T. S.; Ferrari, A. C. Quantifying Defects in Graphene *via* Raman Spectroscopy at Different Excitation Energies. *Nano Lett.* **2011**, *11*, 3190–3196.
39. Simmons, J. G. Generalized Formula for the Electric Tunnel Effect between Similar Electrodes Separated by a Thin Insulating Film. *J. Appl. Phys.* **2004**, *34*, 1793–1803.
40. Wittstock, A.; Biener, J.; Bäumer, M. Nanoporous Gold: A New Material for Catalytic and Sensor Applications. *Phys. Chem. Chem. Phys.* **2010**, *12*, 12919–12930.
41. Zhang, X. W.; Pan, Y.; Zheng, Q.; Yi, X. S. Time Dependence of Piezoresistance for the Conductor-Filled Polymer Composites. *J. Polym. Sci., Polym. Phys.* **2000**, *38*, 2739–2749.
42. Lu, J. R.; Weng, W. G.; Chen, X. F.; Wu, D. J.; Wu, C. L.; Chen, G. H. Piezoresistive Materials from Directed Shear-Induced Assembly of Graphite Nanosheets in Polyethylene. *Adv. Funct. Mater.* **2005**, *15*, 1358–1363.
43. Al-Solamy, F. R.; Al-Ghamdi, A. A.; Mahmoud, W. E. Piezoresistive Behavior of Graphite Nanoplatelets Based Rubber Nanocomposites. *Polym. Adv. Technol.* **2012**, *23*, 478–482.
44. Herrmann, J.; Muller, K. H.; Reda, T.; Baxter, G. R.; Raguse, B.; de Groot, G. J. J. B.; Chai, R.; Roberts, M.; Wieczorek, L. Nanoparticle Films as Sensitive Strain Gauges. *Appl. Phys. Lett.* **2007**, *91*, 183105.
45. Li, X. S.; Zhu, Y. W.; Cai, W. W.; Borysiak, M.; Han, B. Y.; Chen, D.; Piner, R. D.; Colombo, L.; Ruoff, R. S. Transfer of Large-Area Graphene Films for High-Performance Transparent Conductive Electrodes. *Nano Lett.* **2009**, *9*, 4359–4363.
46. Metzger, C.; Fleisch, E.; Meyer, J.; Dansachmuller, M.; Graz, I.; Kaltenbrunner, M.; Keplinger, C.; Schwodiauer, R.; Bauer, S. Flexible-Foam-Based Capacitive Sensor Arrays for Object Detection at Low Cost. *Appl. Phys. Lett.* **2008**, *92*, 013506.
47. Manunza, I.; Sulis, A.; Bonfiglio, A. Pressure Sensing by Flexible, Organic, Field Effect Transistors. *Appl. Phys. Lett.* **2006**, *89*, 143502.